Interpenetrating spiral vortices and other coexisting states in suspension Taylor-Couette flow

Prashanth Ramesh ® and Meheboob Alam ®*

Jawaharlal Nehru Centre for Advanced Scientific Research, Jakkur PO, Bangalore 560064, India

We report interpenetrating spiral vortices (ISVs), a coexisting state of upward and downward propagating spiral/helical vortices, in a neutrally buoyant suspension undergoing Taylor-Couette flow, with the inner cylinder rotating and the outer cylinder at rest. Along with ISV and Taylor vortex flow (TVF), the nonaxisymmetric patterns, such as the wavy Taylor vortices (WTVs) and spiral vortex flows (SVFs), and the coexisting states of "TVF+WTV" and "TVF+SVF" are also uncovered. It is shown that the "TVF+SVF" pattern appears as a primary transition, which gives birth to interpenetrating spirals as a secondary transition beyond a critical Reynolds number, with the final state being that of WTVs over a range of particle volume fractions and Reynolds number.

Introduction. The well-known Taylor-Couette flow (TCF) has been used for studies on hydrodynamic stability, flow transitions, and the route to chaos and turbulence [1–11]. The Taylor-Couette (TC) setup also served as a prototype experimental system to uncover new instability modes in complex fluids; for example, the purely elastic instabilities [12] were uncovered with dilute polymer solutions, and Taylor-like vortices were found in a shear banded flow of wormlike micelles [13]; several nonaxisymmetric patterns and two coexisting states of stationary and traveling waves were reported in recent works [14,15] on the TCF with noncolloidal suspensions. Majji *et al.* [14] carried out detailed flow visualization experiments with neutrally buoyant suspensions of spherical particles in a TC setup, with only the inner cylinder rotating. Prior works on a similar TC setup with Newtonian fluids [3,8] established that, with increasing Reynolds number, the flow transitions from the "finite" circular Couette flow (the acronym "CCF" will henceforth be used to refer to the flow in a finite-height TC cell which is embodied with Ekman vortices near end plates [3,4] at nonzero rotation rates) to azimuthally invariant stationary Taylor vortex flow (TVF), to azimuthally propagating wavy Taylor vortex (WTV), to modulated WTV flows beyond which featureless turbulence sets in; it must be noted that the underlying bifurcation scenario in any finite-height TC cell belongs to the class of "imperfect" bifurcations [4,9,10] in contrast to the "perfect" bifurcation scenario that holds in the ideal case of infinite cylinders. Along with TVF and WTV, Majji *et al.* [14] discovered three nonaxisymmetric flow states, namely, (i) the spiral vortex flow (SVF), (ii) wavy spiral vortices, and (iii) ribbons (RIB), which are completely absent in a pure Newtonian fluid (with only inner cylinder rotating).

Recently we carried out experiments on suspension TCF [15] that includes (i) simultaneous flow visualization and torque measurements and (ii) the velocity measurements using particle image velocimetry (PIV). For dilute suspensions with particle volume fractions of $\phi < 0.05$, the bifurcation scenario was found to be the same (CCF↔TVF↔WTV) as in the Newtonian case, with a slight decrease in critical Reynolds number for the CCF to TVF transition with increasing

---

*meheboob@jncasr.ac.in

particle loading. At $\phi \geqslant 0.05$, however, the nonaxisymmetric SVF pattern appeared as a primary bifurcation from the CCF state during down-sweep experiments, resulting in a pattern-transition route of "WTV→TVF→SVF→CCF" with decreasing rotation rate. With increasing inner-cylinder rotation, two new "coexisting states," namely, the "WTV+TVF" and "TVF+SVF," were found over a range of (Re, ϕ). Continuing the above experiments, here we report a new pattern, called the interpenetrating spiral vortices (ISVs), and analyze its characteristic features and the underlying bifurcation scenario. We also show that the sequence of pattern transitions with increasing/decreasing Re is qualitatively different compared to our previous work [15] and Ref. [14].

Experimental setup and method. Our TC setup consists of two concentric cylinders mounted on an Anton-Paar MCR-302 rheometer. The inner cylinder, made of anodized aluminum, has a radius of $r_i = 16$ mm and the outer cylinder, made of acrylic (of refractive index $n = 1.49$), has a radius of $r_o = 17$ mm, yielding a gap width of $\delta = r_o - r_i = 1.0$ mm. The height of the inner cylinder is $h = 16.5$ mm, and hence the aspect ratio of the present TC cell is $\Gamma = h/\delta = 16.5$, about 1.5 times larger than the maximum aspect ratio $\Gamma = 11$ of our previous setup [15]; the radius ratio is $\eta = r_i/r_o = 0.94$ and the curvature of the cell is $\kappa = \delta/R_i = 0.0625$; both are closer to the limiting case ($\eta \to 1$ and $\kappa \to 0$) of plane Couette geometry. The polymethyl methacrylate (PMMA) microspheres (with a mean diameter of $d_p = 40 \pm 5$ μm, the material density of $\rho_p = 1180$ kg m^{-3}, and the refractive index of $n_p = 1.4873$) are suspended in a density and refractive-index matched solvent (a ternary mixture of water, glycerine, and ammonium thiocyanate NH$_4$SCN) having an intrinsic density of $\rho = 1182.16$ kg m$^{-3} \approx \rho_p$ and a refractive index of $n = 1.4884 \approx n_p$. The measured suspension viscosity [15] was found to be in close agreement with the Krieger-Dougherty relation, $\mu(\phi) = \mu_l[1 - \phi/\phi_m]^{-\beta}$, where $\mu(0) \equiv \mu_l = 6.846$ mPa s (at $T = 22$ °C) is the shear viscosity of the solvent, $\phi_m = 0.585$ is the maximum packing fraction, and $\beta = 2$. The first and second normal-stress differences were found to be negligible [15] over the range of $\phi \leqslant 0.2$. The flow Reynolds number, based on the suspension viscosity $\mu(\phi)$, is calculated from Re $= \rho \omega_i r_i \delta/\mu(\phi)$, where $\omega_i r_i$ is the rotational velocity of the inner cylinder.

The rotational frequency of the inner cylinder was varied from $f = \omega_i/2\pi = 1$ Hz to $f = 20$ Hz, which corresponds to a variation in the apparent shear rate over $\dot{\gamma} \in (3, 1410)$ s^{-1} that was calculated by the software Rheoplus-v3.62, connected with our rheometer. For the range of $\dot{\gamma}$ accessed in our experiments, the particle Reynolds number, the Stokes number, and the Péclet number are given by Re$_p = \rho_p \dot{\gamma} d_p^2/4\mu_l = 6.9 \times 10^{-5}\dot{\gamma} \in (10^{-4}, 0.1)$, St $= \dot{\gamma}\tau_v = (2/9)Re_p \in (10^{-5}, 0.02)$, and Pe $= 3\pi \mu_l d_p^3 \dot{\gamma}/4k_B T \in (10^5, 10^8)$, where $\tau_v = m_p/3\pi \mu_l d_p$ is the viscous relaxation time of a single particle and k_B is the Boltzmann constant. These values are of the same order as in Ref. [15]. We conclude that the suspension particles are non-Brownian (Pe $\gg 1$), the fluid-particle interactions are strong (St $\ll 1$), and the particle inertia may be neglected (Re$_p < 0.1$) near the onset of non-CCF patterns. In the present experiments, the free surface boundary condition holds at the top of the TC cell. A 5-W LED lamp was used to illuminate a TC cell, and the anisotropic green mica flakes were added to the suspension, with a seeding level of $< 0.15\%$ by volume, to aid the visualization of the flow. The images of flow patterns were captured with a Nikon D750 DSLR camera, fitted with a 105-mm Nikkor macro lens and a polarizer.

Results and discussion. For a pure Newtonian fluid ($\phi = 0$), typical surface patterns of Taylor vortices and wavy Taylor vortices are displayed in Figs. 1(a) and 1(b), respectively; on the right of each snapshot, we have added the corresponding space-time evolution that has been constructed from the videos (captured by the same camera at 60 fps) by considering a strip of 1 pixel width along the cylinder height over a time window of 4 s. With reference to Fig. 1(b), the fast Fourier transform (FFT) of the time series of pixel intensities at different axial heights (see Figs. S.1(a)– S.1(c) in the Supplemental Material [16]) confirmed the propagating nature of these vortices, having a wave speed of $\omega/\omega_i \approx 0.5$. On the other hand, the temporal invariance of the space-time diagram displayed on the right side of Fig. 1(a) confirms the stationary nature of Taylor vortices. For the latter case, an FFT analysis, similar to Fig. S.1 in Ref. [16], confirmed that the related power spectra is featureless (not shown).
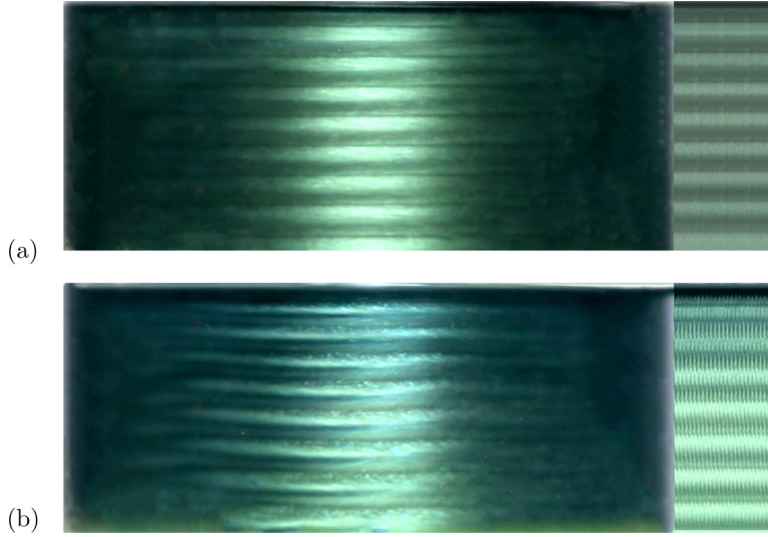
FIG. 1. Flow patterns for a Newtonian fluid ($\phi = 0$) at (a) Re = 170 (TVF, Taylor Vortex Flow) and (b) Re = 210 (WTV, Wavy Taylor Vortex); other parameters are $\Gamma = 16.5$ and $\eta = 0.94$. On the right of each panel, the space-time diagram across the cylinder-height over a time-window of 4 seconds is superimposed; see the text (and Fig. S.1 in Supplementary Material [16]) for details.

The complete phase diagrams of patterns in the (Re, ϕ) plane are displayed in Fig. 2 for both up-sweep [panel (a)] and down-sweep [panel (b)] experiments. The symbols indicate the onset of various flow patterns when Re is varied quasistatically for a given ϕ; note that all presented results are based on independent up-sweep and down-sweep runs. In both cases, each experiment is started with a well-mixed suspension in the annular gap, and the rotation rate of the inner cylinder is increased quasistatically from $\omega_i = \omega_i^{\min}$ (up-sweep) or decreased from $\omega_i = \omega_i^{\max}$ (down-sweep)
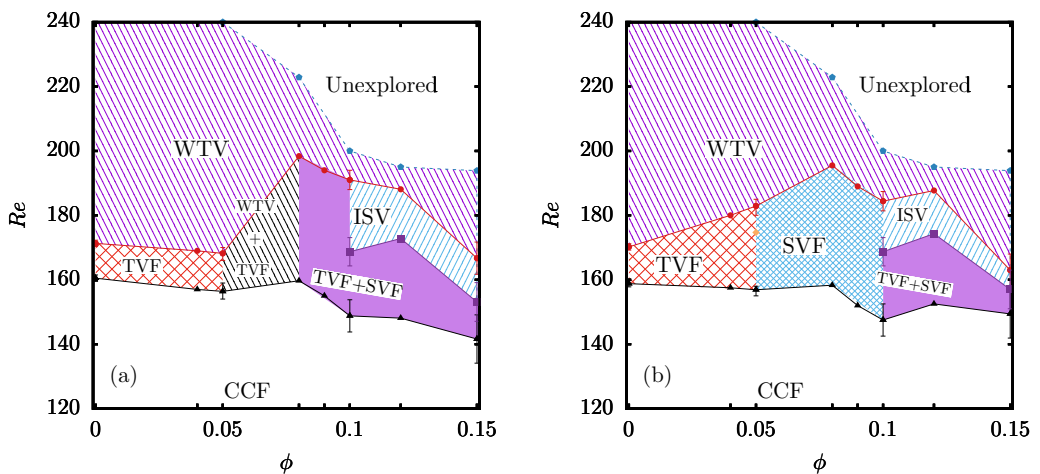

FIG. 2. Phase diagrams of patterns in the (Re, ϕ) plane for (a) up-sweep and (b) down-sweep runs. Different states are classified as CCF (circular Couette flow in a "finite" TC cell), TVF (Taylor vortex flow), WTV (wavy Taylor vortex), SVF (spiral vortex flow), and ISV (interpenetrating spiral vortex). The error bars at $\phi = 0.05$, 0.1, and 0.15 represent the maximum variation among three different runs.

linearly at a specified ramp rate of $d\,\mathrm{Re}/d\tau = 0.0066$ [where $\tau = t/t_d$ and $t_d = \rho\delta^2/\mu(\phi)$ is the diffusion timescale]; the invariance of pattern transition on the ramp rate was checked by repeating experiments with a higher ramp rate of $d\,\mathrm{Re}/d\tau = 0.055$—our lowest ramping rate of $d\,\mathrm{Re}/d\tau = 0.0066$ is smaller by a factor of about 50 than those employed in Refs. [14,15]. Although tracking the bifurcation points via such quasistatic protocol needs extreme care, especially to locate Hopf bifurcations for the onset of oscillatory modes [17], we believe the above two ramping rates (that differ by an order of magnitude) are slow enough to correctly identify pattern transitions in the present system. In any case, the white region in the top right corner of Figs. 2(a) and 2(b) remains unexplored, since the maximum rotation frequency of the inner cylinder in our setup is $f_i^{\max} = 20$ Hz and the maximum achievable inner-cylinder rotation depends on the particle loading (since the effective viscosity of the suspension increases with increasing ϕ); for example, the rotational frequencies of $f_i = 12.0$ Hz (i.e., $\omega_i = 2\pi f_i = 75.4\,\mathrm{s}^{-1}$) and 16.6 Hz ($\omega_i = 104.3\,\mathrm{s}^{-1}$) at $\phi = 0$ and 0.1, respectively, correspond to a Reynolds number of $\mathrm{Re} \approx 200$.

The lines marked by different symbols in Figs. 2(a) and 2(b) denote approximate phase boundaries between two different patterns; in general, the critical Reynolds number $\mathrm{Re_{cr}}$ for the onset of various non-CCF states decreases with increasing ϕ, which has also been verified from simultaneous torque measurements at the inner cylinder in the same rheometer (not shown). It is clear from Fig. 2 that, for a pure Newtonian fluid ($\phi = 0$), the primary bifurcation leads to TVF [such as Fig. 1(a)] at $\mathrm{Re} \approx 160$ and on further increase in Re, the WTV [such as Fig. 1(b)] is born at $\mathrm{Re} \approx 171$. While the Taylor vortices are azimuthally invariant and appear via a pitchfork bifurcation from the CCF state, the WTV breaks the azimuthal rotational symmetry [SO(2)] and appears via a hysteretic [15] Hopf bifurcation. The overall pattern transition of "CCF→TVF→WTV" with increasing Re holds also in a dilute suspension ($\phi < 0.05$), but the critical Reynolds number $\mathrm{Re_{cr}}(\phi)$ decreases slightly with increasing particle loading [14,15]. For both cases, the primary bifurcation (CCF→TVF) is found to be imperfect since the measured torque at the inner cylinder (not shown) varied smoothly with Re as the CCF state transitions into other patterns; this finding is similar to that in our previous work [15] and is a consequence of the axial boundary conditions in finite aspect-ratio TC cells.

Beyond particle volume fractions of $\phi \geqslant 0.05$, two coexisting states, namely, (i) WTV+TVF [Fig. 2(a)] and (ii) "SVF+TVF" [Figs. 2(a) and 2(b)], appear as primary bifurcations from the CCF state over the range of $\phi \leqslant 0.2$ studied. The space-time evolution of the SVF+TVF pattern can be ascertained from the left panel of Fig. 3(a), with its snapshot being displayed in Fig. 3(b); the particle volume fraction is $\phi = 0.1$ and the Reynolds number is $\mathrm{Re} = 153$. Note that the spiral vortices represent helicoidal waves [3,8,18] that propagate along and around the cylinders; it rotates in the azimuthal direction while propagating along the axial direction. It is clear from the left panel of Fig. 3(a) that the spiral vortices (near the bottom part of the TC cell) are propagating in the downward direction (which is denoted by SVF^+, following the convention of right-handed helices) that coexist with an array of stationary Taylor vortices near the top. The FFT analysis of the space-time plots of the pixel intensities at axial heights of $z/\delta = 2$, 9, and 13 (see, for details, Fig. S.3 in Ref. [16]) confirmed that while the upper part of Fig. 3(b) represents stationary TVF, the power spectra from $z/\delta = 2$ and 9 contain a characteristic frequency of $\omega/\omega_i \approx 0.49$, indicating the propagating nature of the SVF on the lower part of the TC cell in Fig. 3(b).

The above SVF+TVF pattern undergoes a secondary transition with increasing Re, giving birth to a new state of "interpenetrating spiral vortex" (ISV) [see the snapshot in Fig. 3(d) at $\mathrm{Re} = 190$]. The corresponding space-time evolution in the middle panel of Fig. 3(a) confirms that the interaction of upward- (SVF^-) and downward-propagating (SVF^+) spirals gives birth to the ISV state in Fig. 3(d). The propagating nature of this mode is captured in the power spectra shown in Fig. 3(e) (see Fig. S.4 in Ref. [16] for related time series), with a dimensionless frequency of $\omega/\omega_i \approx 0.462$. Note that the SVF^+ and SVF^- are mirror images of each other under reflection $z \to -z$; their interaction results in a "defect" which is visible near the mid-height in Fig. 3(d). With further increasing Re, the wavy Taylor vortices [such as in Fig. 1(b)] appear along the height of the TC
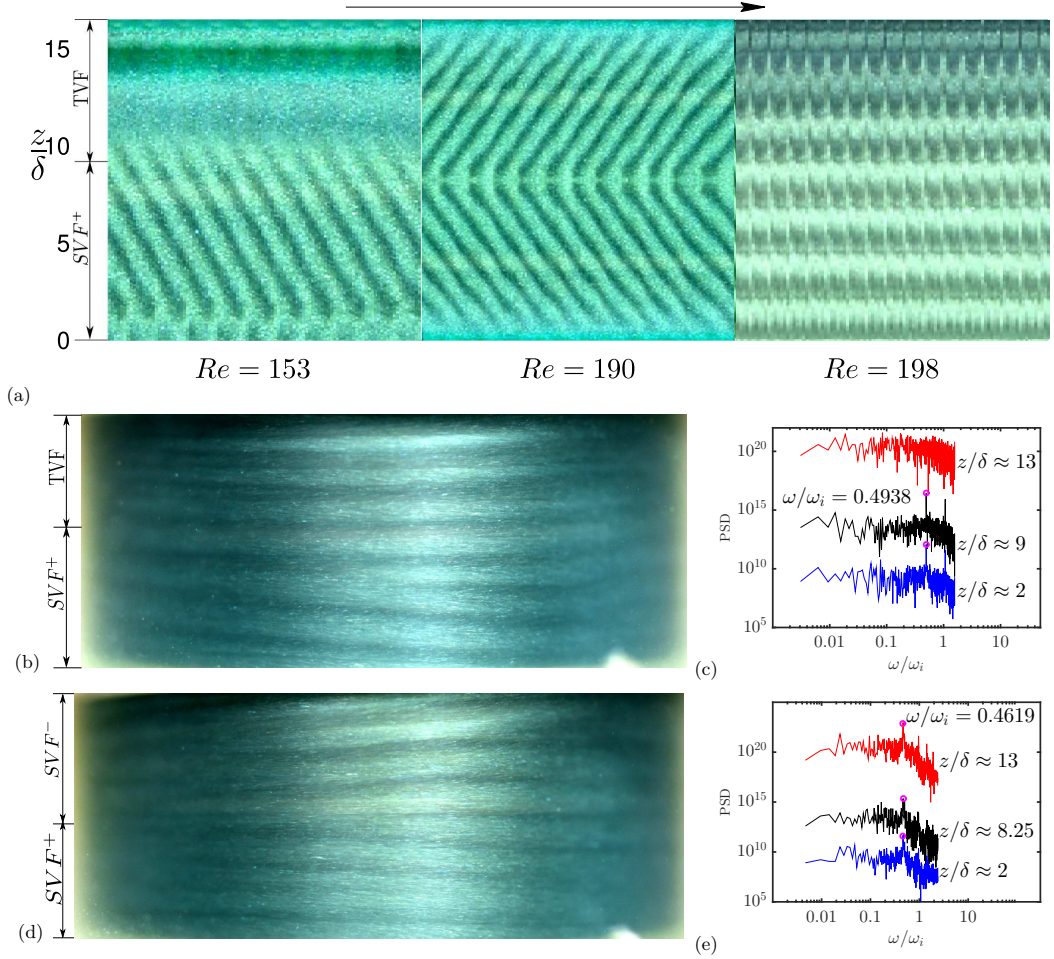
FIG. 3. (a) Space-time diagrams during up-sweep runs at Re = 153 (TVF+SVF, left panel), Re = 190 (ISV, middle panel) and Re = 198 (WTV, right panel). Each panel refers to a time-window of about 4s which has been constructed by stacking 1000 images, each of which represents pixel-intensities over a vertical strip of 4-pixels width; see Fig. S.2 in the Supplementary Material [16] for the same image constructed with a vertical strip of 1-pixel width. (b,c) Snapshot of (b) 'TVF+SVF' at Re = 153 (left-most panel in the top row) and (c) its power spectra. (d,e) Snapshot of (d) ISV (interpenetrating spiral vortex) at Re = 190 (the second panel in the top row) and (e) its power spectra. The ordinates of different curves in panels (c, e) have been shifted for clarity. The particle volume fraction is $\phi = 0.1$.

cell; the spectral characteristics of WTV in suspension TCF are found to be similar [see Figs. S.1(d) and S.1(e) in Ref. [16]] to that in a pure Newtonian fluid. Recall from Fig. 2(b) that the flow, during the ramp-down experiments at $\phi = 0.1$, is initially in the WTV state at Re = 210, which transitions into a sequence of different patterns: (i) ISV at Re $\approx$ 181, (ii) TVF+SVF at Re $\approx$ 168, and (iii) CCF state at Re $\leqslant$ 147; the reverse sequence of transitions (CCC→TVF+SVF→ISV→WTV) is found during ramp-up experiments at $\phi \geqslant 0.1$ [see Fig. 2(a)]. We conclude that the origin of ISV is tied to a secondary transition from the TVF+SVF state during both up-sweep and down-sweep protocols at $\phi \geqslant 0.1$, with the primary transition being "CCF→TVF+SVF." Note that there is a crucial difference of ISV with "ribbons" reported in Ref. [14]: two oppositely propagating (SVF^+ and SVF^-) spirals, originating from two end plates, invade each other and thereby yields a ribbonlike
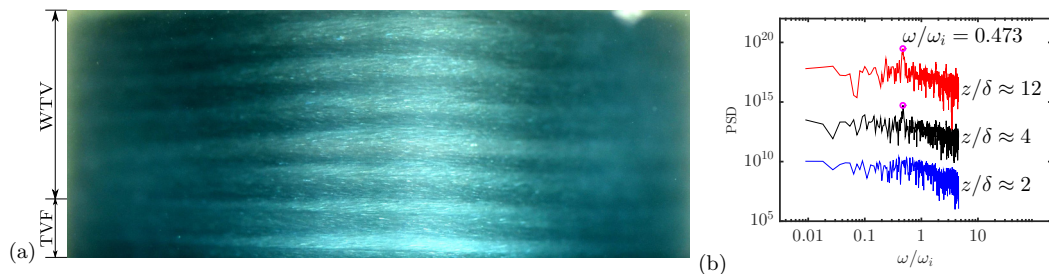
FIG. 4. (a) Snapshot of "WTV+TVF" (Re = 165, $\phi = 0.05$) and (b) the power spectra of the time series of pixel intensities at three axial locations $z/\delta = 2$, 4, and 12 (see, for related details, Fig. S.5 in Ref. [16]); the ordinates of different curves in panel (b) have been shifted for clarity.

pattern; on the other hand, the present experiments with a free surface always led to the nucleation of both SVF^+ and SVF^- near the mid-height of the TC cell [see the middle panel of Fig. 3(a)] which propagate in opposite directions, resulting in an ISV. Moreover, the present finding of the primary transition/bifurcation (CCF→SVF+TVF, with Re ↑) should be contrasted with our previous work [15] that yielded a TVF+SVF state as a secondary transition (CCF→SVF→SVF+TVF; see Fig. 5(a) in Ref. [15]) from the SVF state. The present overall pattern-transition scenario also differs qualitatively from "CCF←RIB←SVF←TVF←WTV" that was uncovered in down-sweep (Re ↓) experiments by Majji *et al.* [14] [contrast their Fig. 21(b) with our Fig. 2(b)] over a range of $0.05 \leqslant \phi \leqslant 0.2$; the roles of top free-surface and finite aspect ratio are further discussed in the concluding paragraph.

Lastly, an example of the coexisting state of WTV+TVF is shown in Fig. 4(a) for $\phi = 0.05$ and Re = 165. The power spectra, obtained from the FFT analysis of the related time series of the pixel intensity at axial heights of $z/\delta = 2$, 4, and 13, are displayed in Fig. 4(b); the details of the related analysis are given in Fig. S.5(a)– S.5(e) of Ref. [16]. It is clear from Fig. 4(b) that the flow is stationary at $z/\delta = 2$, but a propagating mode, having a characteristic frequency of $\omega/\omega_i \approx 0.473$, persists at both $z/\delta = 4$ and 13. This analysis confirms that the bottom part of the TC cell in Fig. 4(a) represents a stationary TVF, while its remaining part is spanned by a traveling mode (WTV).

To further verify the speed of different propagating modes (WTV/SVF/ISV), separate experiments were carried out to capture the scattered-light intensity spectra over about 1/4 axial wavelength (around the center of the TC cell) to construct a time series, and the FFT of this time series gives the wave speed. Figures 5(a) and 5(b) display the power spectra of the scattered-light intensity in the WTV and ISV regimes at $\phi = 0.04$ and $\phi = 0.1$, respectively, for a Reynolds number
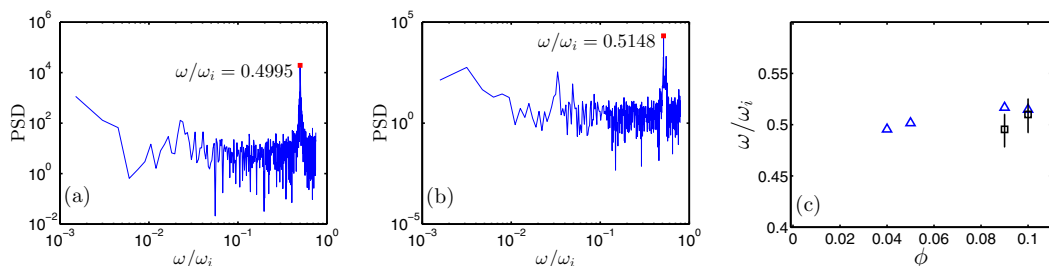

FIG. 5. (a),(b) Power spectra of scattered light intensity at (a) $\phi = 0.04$ (WTV) and (b) $\phi = 0.1$ (ISV), with Re = 180. (c) Normalized wave speed versus ϕ for different modes at Re = 180: $\phi = 0.04$ (WTV), $\phi = 0.05$ (WTV+TVF), $\phi = 0.09$ (TVF+SVF), and $\phi = 0.1$ (ISV). Triangles and squares represent wave speeds of spiral vortices as calculated from light intensity spectra and Hough transform [15], respectively.

of Re = 180 (viz., Fig. 2). This wave speed, normalized by the speed of rotation of the inner cylinder, is plotted versus particle volume fraction in Fig. 5(c) for different propagating modes (WTV: $\phi = 0.04$; WTV+TVF: $\phi = 0.05$; TVF+SVF: $\phi = 0.09$; ISV: $\phi = 0.1$). The robustness of these measurements was also checked by computing the wave speed of SVF and ISV by using Hough transform [15]. The related data are marked by black squares in Fig. 5(c), which confirms that the wave speed is approximately equal to half of the rotation speed of the inner cylinder, irrespective of the type of the propagating modes (WTV/SVF/ISV), having a weak dependence on ϕ.

In conclusion, we uncovered ISVs during both up-sweep (increasing *Re*) and down-sweep (decreasing Re) protocols over a range of particle volume fractions $\phi \in (0.08, 0.15)$. While the ISVs have been reported in "counter-rotating" Newtonian TCF [3,8], their appearance in suspension TCF with only inner-cylinder rotating is a novel finding. In addition, the nonaxisymmetric patterns, such as the wavy vortices and spiral vortices, and the coexisting states of WTV+TVF and TVF+SVF [15] have also been confirmed. In contrast to Ref. [15], we showed that the TVF+SVF pattern appears as a primary transition during both up-sweep and down-sweep experiments, which gives birth to interpenetrating spirals as a secondary transition beyond some critical Reynolds number. The final state at large enough Re is found to be that of WTV (Fig. 2) over the range of $\phi \leqslant 0.2$ and Re $\leqslant 200$. The latter transition ISV→WTV is fundamentally different from the well-known route of transition to "spiral" turbulence (ISV→SPT) [8] in counter-rotating Newtonian TCF for which interpenetrating spirals act as progenitors of turbulent bursts [19] before spiral turbulence sets in. Collectively, the present and previous [15] works confirmed that all coexisting states, including ISV, persist in suspension TCF if the aspect ratio is larger than some moderate value $\Gamma \geqslant 7.3$ (Fig. 12 in Ref [15]) and if the radius ratio, $\eta \geqslant 0.877$, belongs to the narrow-gap limit (Fig. 13 in Ref [15]). The top surface of the TC cell being "free" or "closed" is not expected to influence the onset of coexisting states as the same has been confirmed previously [15] via both (i) image analysis and (ii) velocity (PIV) measurements (Figs. 22 and 23 in Ref. [15]). A mechanistic understanding of the origin of all coexisting patterns would require stability analyses; that the primary bifurcation in suspension TCF with a rotating inner cylinder results in nonaxisymmetric and mixed states (SVF/ISV/SVF+TVF/WTV+TVF) at $\phi \geqslant 0.05$ paves the way for future theoretical predictions based on continuum models of suspensions. It would be interesting to carry out experiments in suspension TCF in small aspect-ratio, $\Gamma = O(1)$, wide-gap TC cells to understand the role of particles and the axial boundary conditions on the so-called anomalous [4–7,9,10] Taylor vortices and the underlying imperfect bifurcation scenario.

[1] G. I. Taylor, Stability of a viscous liquid contained between two rotating cylinders, Philos. Trans. R. Soc., A **223**, 289 (1923).

[2] G. I. Taylor, Fluid friction between rotating cylinders I—Torque measurements, Proc. R. Soc. London, Ser. A **157**, 546 (1936).

[3] D. Coles, Transition in circular Couette flow, J. Fluid Mech. **21**, 385 (1965).

[4] T. B. Benjamin, Bifurcation phenomena in steady flows of a viscous fluid, Proc. R. Soc. London, Ser. A **359**, 27 (1978).

[5] T. Mullin and T. B. Benjamin, Transition to oscillatory motion in the Taylor experiment, Nature (London) **288**, 567 (1980).

[6] A. Lorenzen, G. Pfister, and T. Mullin, End effects on the transition to time-dependent motion in the Taylor experiment, Phys. Fluids **26**, 10 (1982).

[7] T. Mullin, Mutations of steady cellular flows in the Taylor experiment, J. Fluid Mech. **121**, 207 (1982).

[8] C. D. Andereck, S. S. Liu, and H. L. Swinney, Flow regimes in a circular Couette system with independently rotating cylinders, J. Fluid Mech. **164**, 155 (1986).

[9] K. A. Cliffe, T. Mullin, and D. G. Schaeffer, The onset of steady vortices in Taylor-Couette flow: The role of approximate symmetry, Phys. Fluids **24**, 064102 (2012).

[10] T. Mullin, M. Heise, and G. Pfister, Onset of cellular motion in the Taylor-Couette flow, Phys. Rev. Fluids **2**, 081901 (2017).

[11] S. Grossmann, D. Lohse, and C. Sun, High–Reynolds number Taylor-Couette turbulence, Annu. Rev. Fluid Mech. **48**, 53 (2016).

[12] R. G. Larson, E. Shaqfeh, and S. Muller, A purely elastic instability in Taylor-Couette flow, J. Fluid Mech. **218**, 573 (1990).

[13] M. A. Fardin, B. Lasne, O. Cardoso, G. Grégoire, M. Argentina, J. P. Decruppe, and S. Lerouge, Taylor-Like Vortices in Shear-Banding Flow of Giant Micelles, Phys. Rev. Lett. **103**, 028302 (2009).

[14] M. V. Majji, S. Banerjee, and J. F. Morris, Inertial flow transitions of a suspension in Taylor-Couette geometry, J. Fluid Mech. **835**, 936 (2018).

[15] P. Ramesh, S. Bharadwaj, and M. Alam, Suspension Taylor–Couette flow: Co-existence of stationary and traveling waves, and the characteristics of Taylor vortices and spirals, J. Fluid Mech. **870**, 901 (2019).

[16] See Supplemental Material at http://link.aps.org/supplemental/10.1103/PhysRevFluids.5.042301 for detailed analyses to support present conclusions based on Figs. 1–4.

[17] G. Pfister and U. Gerdts, Dynamics of Taylor wavy vortex flow, Phys. Lett. A **83**, 23 (1981).

[18] Ch. Hoffmann, M. Lücke, and A. Pinter, Spiral vortices and Taylor vortices in the annulus between rotating cylinders and the effect of an axial flow, Phys. Rev. E **69**, 056309 (2004).

[19] K. Coughlin and P. S. Marcus, Turbulent Bursts in Couette-Taylor Flow, Phys. Rev. Lett. **77**, 2214 (1996).